

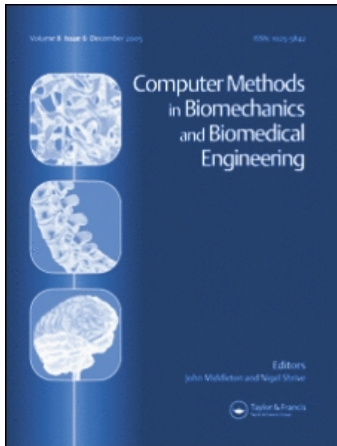
This article was downloaded by: [Zimmer Research Library]

On: 24 February 2009

Access details: Access Details: [subscription number 789040299]

Publisher Taylor & Francis

Informa Ltd Registered in England and Wales Registered Number: 1072954 Registered office: Mortimer House, 37-41 Mortimer Street, London W1T 3JH, UK



Computer Methods in Biomechanics and Biomedical Engineering

Publication details, including instructions for authors and subscription information:

<http://www.informaworld.com/smpp/title-content=t713455284>

Quantifying nonlinear anisotropic elastic material properties of biological tissue by use of membrane inflation

Jeffrey E. Bischoff^a; Elizabeth S. Drexler^b; Andrew J. Slifka^b; Christopher N. McCowan^b

^a Zimmer, Inc., Warsaw, IN, USA ^b Materials Reliability Division, NIST, Boulder, CO, USA

First Published on: 09 February 2009

To cite this Article Bischoff, Jeffrey E., Drexler, Elizabeth S., Slifka, Andrew J. and McCowan, Christopher N. (2009) 'Quantifying nonlinear anisotropic elastic material properties of biological tissue by use of membrane inflation', *Computer Methods in Biomechanics and Biomedical Engineering*,

To link to this Article: DOI: 10.1080/10255840802609420

URL: <http://dx.doi.org/10.1080/10255840802609420>

PLEASE SCROLL DOWN FOR ARTICLE

Full terms and conditions of use: <http://www.informaworld.com/terms-and-conditions-of-access.pdf>

This article may be used for research, teaching and private study purposes. Any substantial or systematic reproduction, re-distribution, re-selling, loan or sub-licensing, systematic supply or distribution in any form to anyone is expressly forbidden.

The publisher does not give any warranty express or implied or make any representation that the contents will be complete or accurate or up to date. The accuracy of any instructions, formulae and drug doses should be independently verified with primary sources. The publisher shall not be liable for any loss, actions, claims, proceedings, demand or costs or damages whatsoever or howsoever caused arising directly or indirectly in connection with or arising out of the use of this material.

Quantifying nonlinear anisotropic elastic material properties of biological tissue by use of membrane inflation

Jeffrey E. Bischoff^{a*}, Elizabeth S. Drexler^b, Andrew J. Slifka^b and Christopher N. McCowan^b

^aZimmer, Inc., Warsaw, IN, USA; ^bMaterials Reliability Division, NIST, Boulder, CO, USA

(Received 6 March 2008; final version received 22 September 2008)

Determination of material parameters for soft tissue frequently involves regression of material parameters for nonlinear, anisotropic constitutive models against experimental data from heterogeneous tests. Here, parameter estimation based on membrane inflation is considered. A four parameter nonlinear, anisotropic hyperelastic strain energy function was used to model the material, in which the parameters are cast in terms of key response features. The experiment was simulated using finite element (FE) analysis in order to predict the experimental measurements of pressure versus profile strain. Material parameter regression was automated using inverse FE analysis; parameter values were updated by use of both local and global techniques, and the ability of these techniques to efficiently converge to a best case was examined. This approach provides a framework in which additional experimental data, including surface strain measurements or local structural information, may be incorporated in order to quantify heterogeneous nonlinear material properties.

Keywords: cardiovascular; inflation; parameter regression; material optimisation

1. Introduction

The mechanical properties of many types of soft tissue (e.g. cardiovascular tissue, tendon/ligament, skin) are critically important to the physiological function of the tissue. Cardiovascular tissue in particular is known to be nonlinear and anisotropic (Humphrey 1995), and these material characteristics, in addition to residual stress, have been shown to impact the function of the tissue within the circulatory system (Delfino et al. 1997). Similarly, pathology of the tissues is frequently accompanied by alteration of the mechanical properties due to structural changes (Beattie et al. 1998), and thus quantification of material properties can serve as a diagnostic tool. Because cells within tissues are able to transduce a mechanical signal into a cellular response, *in vitro* systems have been used to explore the evolution of structure and material properties in response to intermittent or sustained loading (Gleason et al. 2007), where again quantification of material properties plays a key role.

Several different modes of deformation have been used to interrogate the nonlinear, anisotropic properties of cardiovascular tissue including uniaxial/biaxial extension (Dixon et al. 2003), suction/aspiration (Ohashi et al. 2005), inflation (Humphrey et al. 1987; Hsu et al. 1994; Zhang et al. 2005; Slifka et al. 2006; Drexler et al. 2007), compression and indentation (Cox et al. 2006). Membrane inflation has been used by numerous investigators, in which mechanical loading is decoupled from specimen

gripping and the mechanical integrity of the tissue in the region of interest is not compromised. Additionally, a single test is sufficient for interrogating anisotropic nonlinear properties because of the multiaxial loading state and the body of strain data that can be measured. On the other hand, extraction of useful results from the raw data requires detailed analysis, including finite element (FE) analysis, and therefore regression of material parameters from resulting pressure versus deformation data is more complex than from a homogeneous deformation mode.

Because of the material complexity of cardiovascular tissue, experimental data are most effectively reduced by implementation of a suitable constitutive model whereby the response is condensed to a discrete set of material parameters. While nonlinear isotropic strain energy functions have been used towards this end (Delfino et al. 1997), nonlinear anisotropic formulations are more consistent with the tissue structure and have had good success in capturing material data (Demiray and Vito 1991; Dixon et al. 2003; VanBavel et al. 2003). With such models however, quantification of the material parameters is not necessarily a straightforward exercise because of the complexity of both the models and the experiment. Inverse FE techniques have been used towards this end, whereby values of the material parameters are varied from analysis to analysis until a reasonable or best fit to the data is realised. Various techniques for updating nonlinear

*Corresponding author. Email: jeff.bischoff@zimmer.com

material parameters for soft tissue characterisation have been used, from manual iteration (Zhang et al. 2005) to automated techniques using optimisation methods including gradient-based approaches (Kyriacou and Humphrey 1997; Holzapfel et al. 2004; Erdemer et al. 2006; Lei and Szeri 2007) and genetic algorithms (Nair et al. 2007). A local best fit can be obtained using automated techniques, but because of the complexity of the material models, local optimisation approaches are critically dependent on an initial guess for the values of the material parameters. Global techniques, on the other hand, more fully explore the parameter space, and thus allow greater confidence that the final set of parameter values truly represents the best fit. The drawback, however, is that global exploration is much more computationally expensive, particularly when dealing with data from experimental tests that require FE analysis.

The goal of the work here was to explore the ability of several optimisation approaches for quantifying the material parameters of vascular tissue through regression against membrane inflation test data. A computational model for the test was developed in which the test metrics (pressure and bubble profile stretch) were predicted by use of a nonlinear anisotropic constitutive model that has been used with success on soft tissue. Two different material optimisation algorithms were used, including a local, gradient-based technique (Levenberg–Marquardt) and a global technique. Finally, the computational approach developed here was applied to a set of data from rat pulmonary arteries, in order to quantify parameters of the tissue.

2. Methods

This work is principally concerned with computational modelling of inflation tests of anisotropic membranes (soft tissue). The motivation derives from membrane inflation tests on vasculature (Drexler et al. 2003, 2007; Slifka et al. 2006) that were conducted in order to quantify material changes between health and disease (hypoxia).

The experimental protocol will be discussed briefly, with appropriate primary references. The bulk of this section will then be devoted to the mathematical analysis including computational modelling, underlying constitutive framework and optimisation algorithms.

2.1 Experimental setup

The experimental system has been described in detail elsewhere (Drexler et al. 2003, 2007). A summary of the setup will be given here, with reference to schematics (including bubble test fixture and computer controlled setup) in Figure 1. Vascular specimens were prepared by excising arterial tissue, slicing the tissue axially to produce a rectangular specimen, trimming connective tissue from the adventitia, and then cutting a roughly 3 mm diameter circular specimen. The specimen was clamped into the test system using an O-ring, and then subjected to inflation. Bubble shape during inflation was imaged using three cameras plus a rotation stage to obtain images at 30° intervals. These intervals were used to determine the orientation at which the bubble profile was maximised; this orientation was reflective of overall material axis alignment. Representative images of the inflated vessel, taken from circumferential and longitudinal perspectives, are shown in Figure 2, illustrating the anisotropy inherent in the material and which is reflected in the deformed profiles. From these images, deformed longitudinal (l_L) and circumferential (l_C) lengths were measured. These lengths were then used to calculate overall profile strains, $\varepsilon_L = \ln(l_L/D)$ and $\varepsilon_C = \ln(l_C/D)$, where $D = 2.318$ mm is the diameter of the aperture in which the vessel is fixed and therefore represents the undeformed profile length.

The uncertainty associated with this system has been previously characterised (Drexler et al. 2007). Measures of length (l_L and l_C), from which profile strains are calculated, were determined to be accurate to within 0.058 mm, and pressure was accurate to within 0.195 kPa. A representative result is shown in Figure 3, in terms

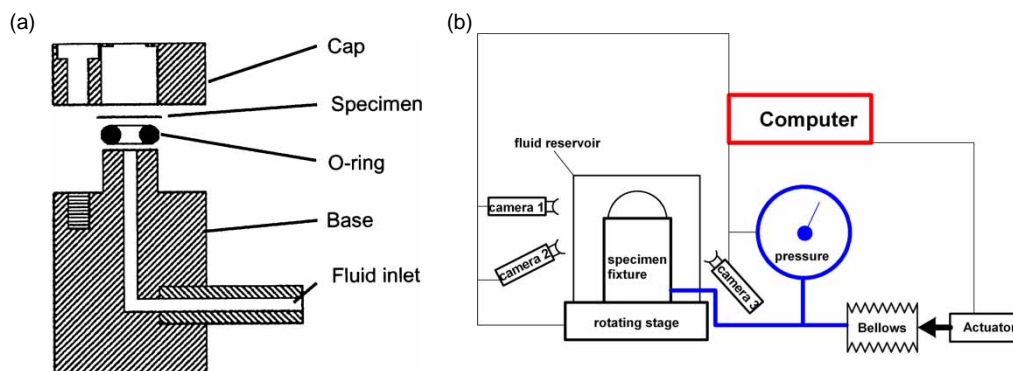


Figure 1. Schematics of the experimental inflation setup. (a) Bubble test fixture. (b) Computer controlled system.

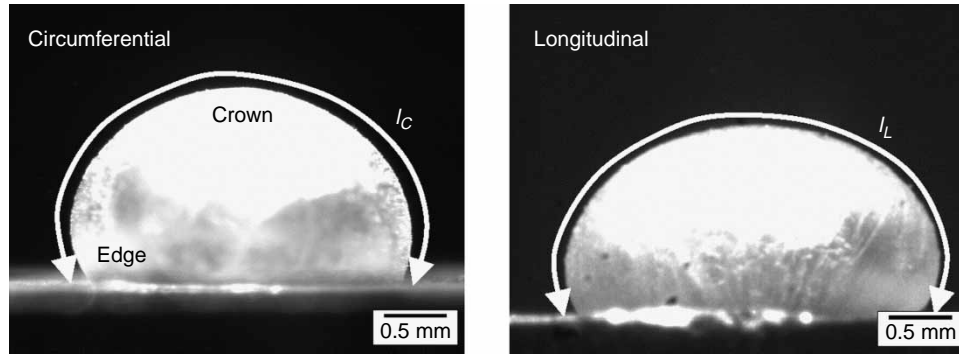


Figure 2. Representative images of inflation from circumferential and longitudinal viewpoints. Note definitions of bubble crown and edge. The deformed profile lengths l_C and l_L are extracted from the images and used to calculate the profile stretches.

of pressure versus profile strain (circumferential and longitudinal). Note that Figure 3 includes the bounds on these data as well, according to the previously mentioned experimental accuracy of the pressure and length measurements. The response is linear for modest pressures/strains, but demonstrates sharp locking behaviour at larger pressures.

2.2 Computational framework

Simulation of the membrane inflation test is based on an accurate representation of the material behaviour, as well as of the boundary value problem. The mathematical constitutive model and its implementation will be described in a subsequent section; here, aspects of the computational boundary value problem will be presented.

All model preparation and analyses were conducted using Abaqus 6.7.¹ Due to typical geometries of the tissues

of interest (thickness less than 0.2 mm, diameters based on test setup of 2.318 mm), membrane conditions were assumed. Accordingly, four node quadrilateral membrane elements (M3D4) were used for all simulations. Nodal displacements were fully constrained along membrane edges, but the edges were allowed to freely rotate during deformation. Note that this is a simplification of the edge conditions in the experimental model, in which the tissue extending beyond the aperture diameter is compressed between the O-ring and fixture, and friction prevents slipping of the tissue during pressurisation. This is therefore one of several modelling assumptions invoked here (including homogeneity of material properties and the governing constitutive model), which could be reconsidered if model results do not compare favourably against experimental data.

A uniform pressure loading was applied to one surface of the membrane; a linear pressure versus time profile was used, although time is fictitious in this case because an elastic constitutive model is used. Prior to inflation, a small perturbation was applied to the central node of the model to initiate deformation and facilitate convergence under subsequent pressure loading. A schematic of the FE model (assuming quarter-plane symmetry) with boundary and loading conditions is shown in Figure 4, along with a representative result following pressurisation.

Profile strain was extracted from the simulations based on the elemental deformations. In particular, given N elements that are equally spaced along the longitudinal and circumferential directions, and recalling the logarithmic strain $\epsilon_i = \ln(\lambda_i)$ (where ϵ_i and λ_i represent logarithmic strain and stretch in a given element, respectively), the overall profile stretch λ is given by

$$\lambda = \frac{1}{N} \sum_{i=1}^N \exp(\epsilon_i).$$

Profile strain from the model was then calculated as

$$\epsilon = \ln \lambda.$$

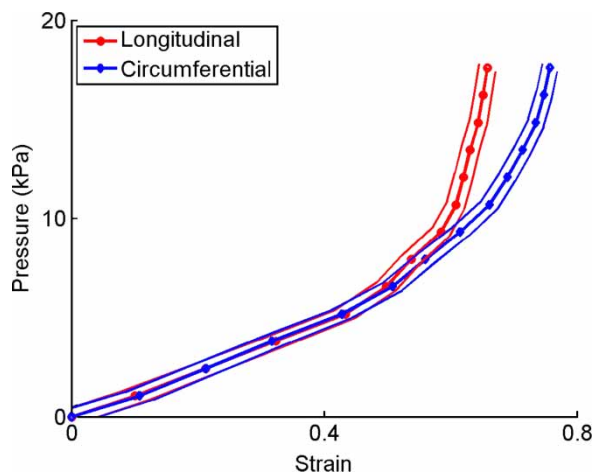


Figure 3. Representative data from bubble inflation tests on vasculature, plotted as applied pressure versus profile strain. Bounds on the data are also plotted, based on the experimental accuracy of the pressure and profile length measurements. This figure is available in colour online.

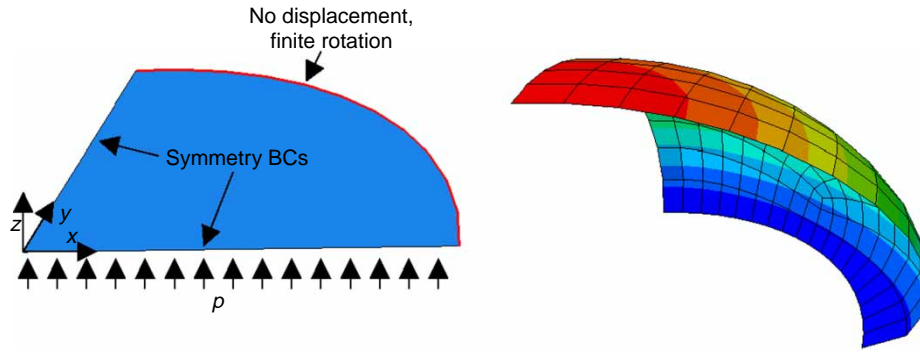


Figure 4. Computational model setup with boundary and loading conditions (left) and representative model result following pressurisation (right); contours reflect membrane displacement in the direction (z) of initial pressurisation. Available in colour online.

In the absence of local measurements of strain, profile strain can be measured experimentally and compared to the model calculation above. In particular, the pressure versus profile strain data measured experimentally were compared to the pressure versus profile strain response of the computational model.

Adequate mesh density was established by comparing the pressure versus profile strain responses along each of the two directions up to a pressure of 25 kPa, using a representative set of parameters (Figure 5). Characteristic element lengths used were $r/3$, $r/6$, $r/12$ and $r/24$, where $r = 1.16$ is the radius (in mm) of the inflation patch. There is little change in system response when decreasing the element length from $r/12$ to $r/24$, as reflected in the R^2 values, and thus a characteristic length no larger than $r/12$ was used in all simulations here. Final meshes for quarter-space models contained approximately 135 elements.

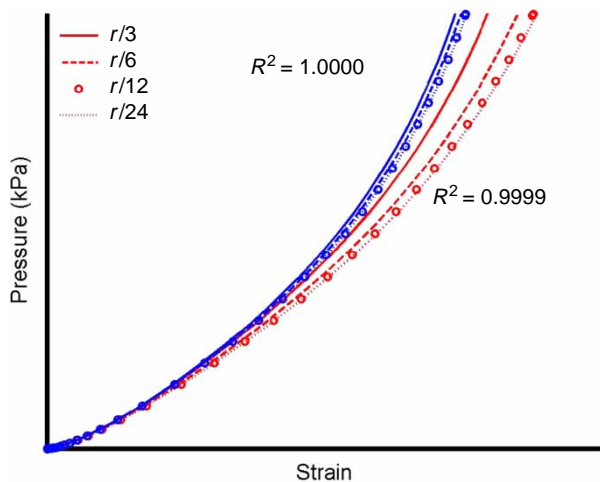


Figure 5. Effect of mesh refinement on the pressure–strain response in the circumferential (red) and longitudinal (blue) directions. The level of mesh resolution is specified by the characteristic element length as a function of the overall patch radius. R^2 values reflect the consistency of the $r/12$ response with the $r/24$ response. Available in colour online.

Misalignment between material axes and anatomical (longitudinal/circumferential) axes was taken into account by rotating material axes relative to the computational model axes (assumed to align with the anatomical axes). When these axes were aligned, or misaligned by a factor of 90° , symmetry considerations allowed for simulation of a quarter space model. For all other alignments, a full model was required. It is expected that in general, material and anatomic axes are coincident.

2.3 Constitutive model

A variety of membranous tissues including vasculature (Holzapfel et al. 2000; Zhang et al. 2005), myocardium (Humphrey et al. 1990) and skin (Fung 1993) are considered to act as nonlinear anisotropic materials in the continuum sense. Several nonlinear anisotropic constitutive models have been proposed for capturing the elastic response of vasculature in particular (Holzapfel et al. 2000; Vito and Dixon 2003; Ohashi et al. 2005); here, the orthotropic eight-chain model is used (Bischoff et al. 2002a) because of its demonstrated ability to capture the nonlinear orthotropic response of a variety of soft tissues including vasculature (Zhang et al. 2005; Drexler et al. 2007) using a small number of material parameters.

Vasculature is widely considered to possess orthotropic material symmetry in which the material axes are aligned with the radial, circumferential and longitudinal material directions (Humphrey 1995; Holzapfel et al. 2000). Recent work treats the media and adventitia as independent, fibre-reinforced composites, with the intima contributing minimally to the overall material response (Holzapfel et al. 2002). Here, the overall effect of the alternating layers of the media is modelled using an orthotropic hyperelastic material model (Bischoff et al. 2002a). While not able to resolve deformation variations due to alternating classes of fibres, this work endeavours to predict, in a global sense, the nonlinear orthotropic material response.

The orthotropic eight-chain model is adapted here for several reasons:

- (1) The original model is cast in terms of material parameters a , b and c that represent the degree of fibre alignment along each of the three material axes. The values of these parameters affect both the degree of anisotropy as well as the locking stretch in the tissue. In order to decouple these effects, the parameter combinations $P = \sqrt{a^2 + b^2 + c^2}/2$, $A = a/P$, and $B = b/P$ are used here. The parameters A and B represent in-plane chain alignment relative to the through-thickness direction and more clearly affect the in-plane anisotropy of the material response; parameter P is directly associated with the amount of crimp in the constituent fibres and impacts the locking stretch of the material without affecting in-plane anisotropy.
- (2) The original model includes a material parameter n that represents macromolecular chain density in units of chain count per unit volume. The initial stiffness of the model is directly correlated with $nk\Theta$ where k is Boltzmann's constant and Θ is absolute temperature. This parameter is now termed $E_0 = nk\Theta$, with units consistent with elastic modulus. Note that this parameter is related to the initial modulus of the material, but as the material model is orthotropic the initial modulus is orientation-specific.
- (3) The original model allowed for variable compressibility through a nonlinear bulk modulus strain energy term. Although for most loading scenarios tissue behaves as an incompressible material, this modelling assumption is useful for computational implementation. Here, since membrane analysis will be used, strict incompressibility of the material is enforced.

The governing equations for the constitutive model, including the elasticity tensor and initial stiffness matrix, are given in the Appendix.

The material model is thus characterised by four material parameters, summarised as follows:

E_0 : Initial material stiffness

A : In-plane fibre alignment along material orientation **a**

B : In-plane fibre alignment along material orientation **b**

P : Locking stretch of a constituent fibre.

The impact of each of the four material parameters on model response to uniaxial tension is shown in Figure 6(a). The benefit of recasting the original model parameters in terms of E_0 , A , B and P is clearly seen here, as each parameter has a largely uncoupled effect on uniaxial material response.

Computational implementation of the mathematical model has been presented elsewhere (Bischoff et al. 2002b). Briefly, the model was incorporated into the commercial FE code ABAQUS 6.7 via a user subroutine that requires the first and second derivatives of the strain energy function (W) with respect to strain (\mathbf{E}), $\partial W/\partial \mathbf{E}$ and $\partial^2 W/\partial \mathbf{E}^2$, respectively. Though this model lends itself to analytical differentiation of the strain energy function, as shown in the Appendix, a more general, numerical differentiation scheme has been incorporated that allows for further expansion into inelastic material models (Bergström et al. 2002; Bischoff et al. 2004).

The sensitivity of the membrane inflation test to the material parameters is shown in Figure 6(b). The impact of each of the parameters on material response is not decoupled as for uniaxial deformation (Figure 6(a)). In particular, altering the values of A and B affects the pressure–strain relationship along both directions, although to different degrees. The impact of adjusting E_0 and P is consistent with what is seen in uniaxial deformation.

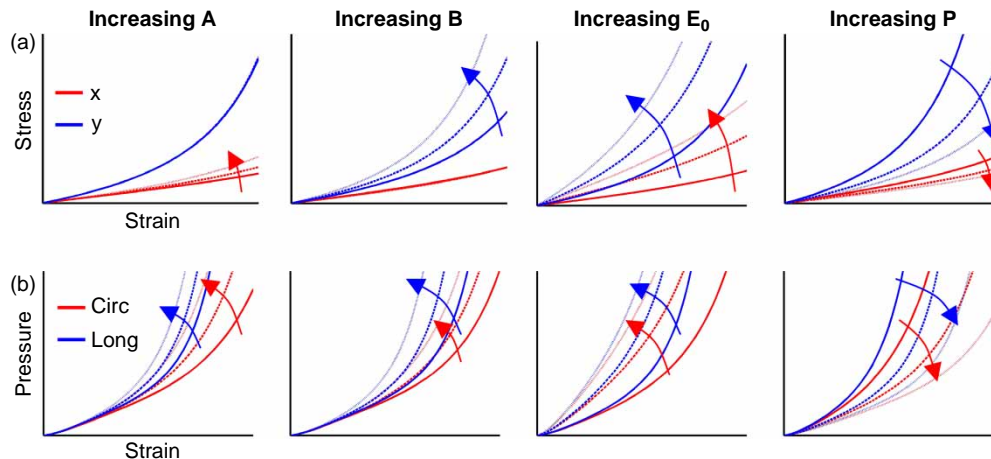


Figure 6. Sensitivity of the model response to the material parameters: (a) uniaxial deformation along the two in-plane material directions (x and y); (b) membrane inflation, as reflected by applied pressure versus profile strain (circumferential and longitudinal). This figure is available in colour online.

2.4 Optimisation procedures

Accurate estimation of material parameters within structural models such as the orthotropic model here is facilitated by the clear relationship between each of the parameters and important aspects of the mechanical response. As seen previously (Figure 6), perturbation of each of the four independent material parameters has a predictable effect on model response to both basic modes of deformation (uniaxial tension) and heterogeneous deformations (membrane inflation). With this knowledge, trial and error estimation of material parameters based on an experimental data set can proceed fairly quickly; for example, an overall stiffer response is obtained by increasing E_0 .

However, for convergence to a set of parameters that provides a best fit in a quantitative sense, nonlinear optimisation techniques can be used. Two approaches were considered here: a gradient-based technique that is restricted to optimising within a localised region of the parameter space and is therefore highly dependent on the initial values of the material parameters; and a global technique that more fully explores the parameter space but at the expense of increased computational cost.

2.4.1 Local optimisation

For convergence to a local best set of parameters, the Levenberg–Marquardt algorithm (Press et al. 1992) has been implemented within an inverse FE approach, as shown schematically in Figure 7. This technique is predicated on a reasonable initial guess of the parameter values. Results from the first analysis were compared to the experimental data. In this case, R -squared values were obtained from the pressure versus strain response in each of the two principal in-plane directions (R_{long}^2 and R_{circ}^2) and summed,

$$R_{\text{total}}^2 = R_{\text{long}}^2 + R_{\text{circ}}^2 \leq 2.$$

If the fit meets a predefined threshold, or successive iterations do not yield an improved fit, no subsequent analyses are required. If the agreement between the model and data is not suitable, the sensitivity of R_{long}^2 and R_{circ}^2 with respect to each of the material parameters (the vector of material parameters is denoted here as \mathbf{p}) must be evaluated, requiring an additional set of FE analyses equal to the number of independent material parameters. The gradient matrix $\nabla \mathbf{R}^2 = \partial \mathbf{R}^2 / \partial \mathbf{p}$ is formulated, where $\mathbf{R}^2 = [R_{\text{long}}^2 \ R_{\text{circ}}^2]^T$. The Hessian matrix $\mathbf{H} = (\nabla \mathbf{R}^2)^T \cdot (\nabla \mathbf{R}^2)$ is then used to update the parameter vector,

$$\mathbf{p}^{(n+1)} = \mathbf{p}^{(n)} + (\mathbf{H} + \alpha \mathbf{I})^{-1} \cdot (\nabla \mathbf{R}^2)^T \begin{bmatrix} 1 - R_{\text{circ}}^2 \\ 1 - R_{\text{long}}^2 \end{bmatrix},$$

where the value of the factor α is iterated to provide the best next set of parameter values. Thus, an additional number

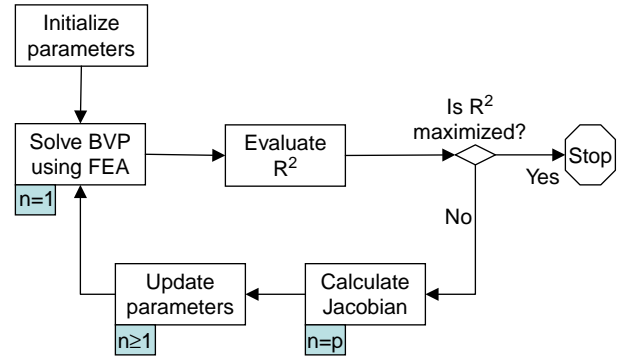


Figure 7. Schematic for material parameter estimation by use of inverse finite element analysis based on the Levenberg–Marquardt algorithm. Shaded boxes indicate the number (n) of FE analyses required at the corresponding step.

of FE simulations is required, depending on the approach for determining α ; each updated set of parameters requires at least $p + 1$ FE solutions of the boundary value problem. Here, iterations continued until R_{total}^2 improved by less than 0.1%.

Python scripting language was used to govern the inverse procedure, including driving the FE analysis (generating appropriate input files and submitting jobs), extracting relevant results from the FE output database, and adjusting material parameters based on the Levenberg–Marquardt algorithm. Calculation of R_{total}^2 required interpolating the model strain predictions to pressure values for which data exist; interpolation and calculation of R_{total}^2 were achieved using a Matlab script, which also was driven by Python. Material parameters were initially estimated by use of a small number of simulations in which the values were updated sensibly based on the anticipated behaviour (Figure 6). These values were the starting points for the optimisation algorithm.

Determination of the starting values is a known critical step in local optimisation. The benefit of using a constitutive model in which the material parameters clearly impact the system response in predictable ways is therefore apparent, as it expedites the trial-and-error process of estimating the initial parameters for the optimisation process. Here, E_0 can be adjusted to approximate the initial stiffness of the response, A and B can be adjusted to approximate the material anisotropy, and finally P can be adjusted to approximate the locking stretch.

2.4.2 Global optimisation

For global optimisation, the commercial software HEEDS (Red Cedar Technology, Inc., East Lansing, MI, USA) was used. This software utilises the proprietary Sherpa algorithm, which spans the parameter space while also achieving local convergence in targeted regions. The Sherpa algorithm provides updated parameter sets

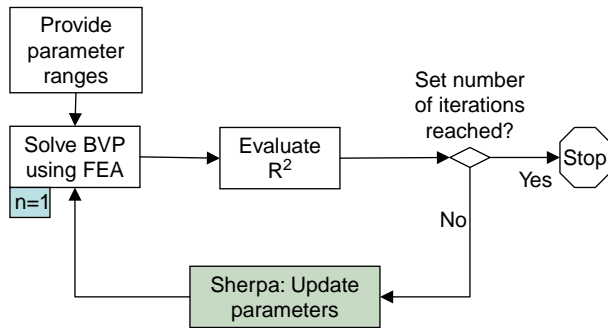


Figure 8. Schematic for global material parameter estimation based on the Sherpa algorithm provided by HEEDS. Only a single FE analysis is required per iteration, but a substantially larger number of iterations is required to establish confidence in the optimisation algorithm, represented by the green shaded box.

based on previous analyses, while the software as a whole interfaces with the various analysis tools including Abaqus and the previously developed Python scripts. The solution approach is shown schematically in Figure 8 in which the Sherpa algorithm is illustrated as a ‘black box’. Only a single FE analysis is required per iteration, but many iterations are needed in order to establish confidence that a global best fit was achieved. Here, the number of iterations was set at 150. The global parameter space for exploration was defined as follows: $0.8 \leq A \leq 1.8$, $0.8 \leq B \leq 1.8$, $1.5 \leq P \leq 2.5$, $5 \leq E_0 \leq 35$ (A , B and P are unitless; E_0 has dimensions of kPa). Continuous variation of these parameters was not utilised during the optimisation process; rather, parameter discretisation for A , B and P was set at 0.01, and for E_0 at 0.3 kPa.

2.4.3 Sequential optimisation

A third approach was also considered here, intended to combine the strengths of both the Sherpa algorithm and gradient-based techniques. Though the Sherpa algorithm is stated to be a hybrid method that combines global and local algorithms, it has been found that a local search following completion of Sherpa improves the final quality of fit. Additionally, inclusion of the local search ensures a local best fit. Accordingly, the final parameter values from the Sherpa process were used as the initial parameter values for a local process. The resulting parameter identification sequence is thus fully automated, and other than user specification of the parameter domain and optimisation controls (e.g. number of iterations), no trial-and-error is required.

2.5 Parameter resolution

The result of the optimisation procedures described above is a single set of material parameters that captures

the experimental data in an objective best sense. However, it is important to understand that there is a domain within the parameter space which includes the optimised parameter set, and that will result in model predictions that are equivalent within the uncertainty of the experimental data. Parameter values cannot be accurately quantified beyond this resolution in a meaningful way.

Here, the resolution of the parameters was established from a representative data set as follows. First, the R -squared values for the upper and lower bounds of the data set shown in Figure 3 were calculated, in both longitudinal and circumferential directions. The difference between the smallest of these values and unity was taken as the effect of experimental accuracy on the R -squared values,

$$\Delta_{R^2} = 1 - \min(R_{\text{upper,long}}^2, R_{\text{lower,long}}^2, R_{\text{upper,circ}}^2, R_{\text{lower,circ}}^2).$$

Then, starting from the optimised set of parameters, each parameter was varied (positively, then negatively) until the R -squared value of the best fit in either direction was reduced by Δ_{R^2} . In particular, A , B and P were varied in increments of 0.01, and E_0 was varied in increments of 0.1 kPa. This approach does not ensure that the model prediction falls within the experimental uncertainty for all data points along the loading curve, but rather determines individual parameter sensitivities that have an overall effect commensurate with the experimental uncertainty.

3. Results

Results here include general observations about the response of anisotropic membranes to inflation, and the use of computational modelling in conjunction with experimental data to determine material parameters.

3.1 Anisotropic membrane inflation – general observations

The goal of membrane inflation analysis is quantification of material properties, presumed to be homogeneous. Data from existing experiments include applied pressure and bubble profile strains versus time. The initial set of results here is designed to justify the use of these data for accurate material parameter estimation.

Figure 9(a) shows the crown stress (circumferential) versus pressure profiles for different values of the initial stiffness E_0 . At small strains (low pressures), there is no dependence of the stress–pressure relationship on stiffness (or any other material property); however, this is not true for nonlinear deformations (large pressures). If the local curvature at large strains is measured at the crown, stress can again be extracted as a function of pressure without determination of material properties

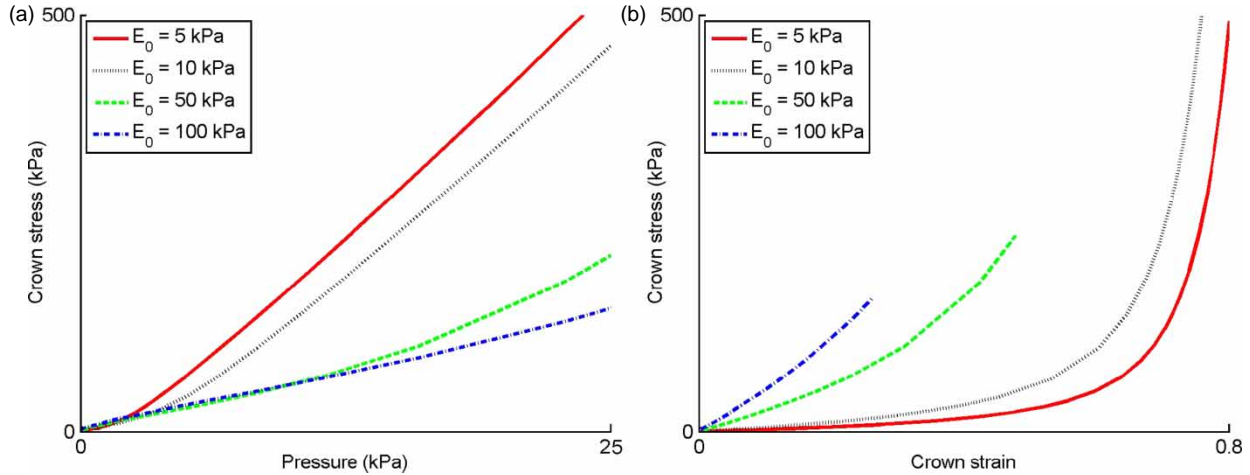


Figure 9. Effect of initial material stiffness on bubble response at the crown: (a) crown stress versus pressure; (b) crown stress versus crown strain. Available in colour online.

by use of analytical techniques (Drexler et al. 2007). Additionally, crown stress versus crown strain (Figure 9(b)) presents sufficient information for resolution of material parameters, but such data are predicated on techniques being available for local measurement of strain. Towards this end, noninvasive techniques exist for measurement of local deformation that could be used within the context of inflation, including digital image correlation (DIC) based on applied speckle patterns (Malcolm et al. 2002; Zhang et al. 2002; Sutton et al. 2008) or tagged magnetic resonance imaging (Augenstein et al. 2005). Use of these systems on the crown would yield both the local biaxial strain state and the local curvature. The curvature and applied pressure would provide the local stress state at the crown; image correlation would provide the local strain state. Regression of material parameters would then rely not on inverse FE analysis of the entire boundary value problem, but rather solely on homogeneous regression against local biaxial stress versus strain data.

The bulk of the work here does not assume the availability of local strain data for the pressurised vessel. Though local curvature can be estimated from the orthogonal bubble profiles, local strain cannot be accurately measured from such profiles. Figure 10 shows local normal strain (symbols) as a function of initial radial location, using four different values of E_0 ; an initial radial location of 0 corresponds to the bubble crown (Figure 2), whereas an initial radial location of r corresponds to the bubble edge. Also shown (solid lines) is the overall profile strain. These results demonstrate that there is variation of local strain along the profile, deviating by over 17% from the overall strain at some locations and by over 10% specifically at the crown. Thus, profile strain can be an unreliable estimate for local crown strain.

3.2 Determination of material parameters

3.2.1 Local approach

Topology of the parameter space is an important issue for local optimisation algorithms including the Levenberg–Marquardt method. Visualisation of the topology is difficult for more than two independent parameters, but snapshots are presented here in Figure 11 in the form of contour plots of R_{total}^2 in reference to a characteristic experimental data set. Unless otherwise indicated in Figure 11, parameter values are as follows: $E_0 = 13$ kPa, $A = 1.2$, $B = 1.1$ and $P = 1.7$. The response surfaces are seen to be smooth in nature, but do not demonstrate well-defined peaks in R_{total}^2 . Because these images are just two-dimensional snapshots, however, effects from the other

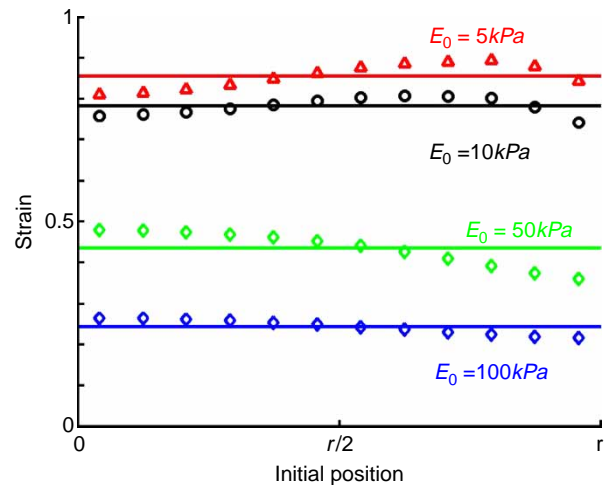


Figure 10. Local strain as a function of initial radial position (symbols) for different values of initial stiffness, as well as overall profile strain (lines).

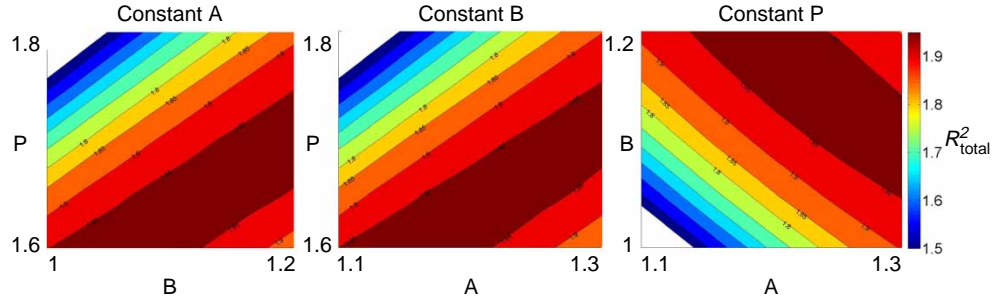


Figure 11. Two-dimensional snapshots of the topology of the parameter space. Available in colour online.

parameters could lead to precise maxima. Local optimisation can be used to more fully explore the topology, starting from a variety of initial parameter sets.

Four separate sets of initial parameter values were used to test the algorithm. Parameter values are summarised in Table 1, as well as details about the convergence process (including final parameter values). The pressure versus strain predictions using the initial starting values are indicated in Figure 12 (left), all demonstrating good fits throughout the pressurisation, particularly in light of experimental uncertainty and modelling assumptions. Also shown in Figure 12 (right) is the difference between the experimental strain and model strain as a function of pressure, in order to draw out differences in the final model predictions. As seen in this figure, the fits are qualitatively different, under- or over-predicting during pressurisation, but rarely missing the data by more than 5% strain. It can thus be concluded that each set of initial parameter values produces a local ‘best fit’ to the experimental data, all of which may be sufficiently accurate in light of the test configuration and overall modelling framework. However, because of the extreme sensitivity of the final result on the initial set of parameters, an overall best-fit can only be obtained by sampling many different sets of parameters.

3.2.2 Global approach

Results from a representative global optimisation process are shown in Figures 13 and 14. The progression of the overall uncertainty estimates (R_{long}^2 , R_{circ}^2 and R_{total}^2) is shown in Figure 13; the progression of the material

parameters is shown in Figure 14. Progression of each of the material parameters is plotted over the pre-defined range of the respective parameter. For this particular data set, an initial optimisation run predicted the value of P to lie on the lower edge of the parameter domain ($P = 1.5$). For this reason, the domain was reset from $1.5 \leq P \leq 2.5$ to $1.0 \leq P \leq 2.0$, and the optimisation performed again; results from this run are shown in the figures. Increasing the allowable number of iterations (150) would be justified if the final best-fit was not yet satisfactory. However, both the uncertainty estimate ($R_{\text{total}}^2 = 1.995$) and the apparent quality of the best fit (Figure 13, inset) suggest that continued iterations are not justified.

Taken together, these preliminary results using local and global approaches motivate a process that establishes confidence that the parameter domain is satisfactorily explored while ensuring that material parameters are accurately resolved. In particular, the global approach is initially used to hone in on a subdomain within the parameter space in which a best fit is anticipated; a local approach is then used to drive the solution to the best set of parameters in that subdomain. Results from this approach will be presented in the next section.

3.3 Comparison to experimental data

Figure 15 shows experimental inflation data from the right pulmonary artery ($n = 6$), left pulmonary artery ($n = 7$), and arterial trunk ($n = 7$) of normotensive rats, as well as the model fits. All model results were obtained by use of the global optimisation described previously followed

Table 1. Summary of initial and final parameter values used during four distinct local optimisation runs.

	Initial parameter values				Following local optimisation					
	A	B	P	E_0 (kPa)	A	B	P	E_0 (kPa)	N	R_{total}^2
Init1	1.10	1.00	1.60	13.0	1.16	1.06	1.68	12.88	3	1.950
Init2	1.30	1.10	1.60	10.0	1.14	1.06	1.58	9.91	11	1.974
Init3	1.20	1.10	1.70	15.0	1.46	1.36	2.42	14.86	11	1.974
Init4	1.30	1.20	1.80	13.0	1.34	1.24	2.02	12.88	6	1.984

Also included are the number of optimisation iterations (N) and the final quality of fit (R_{total}^2).

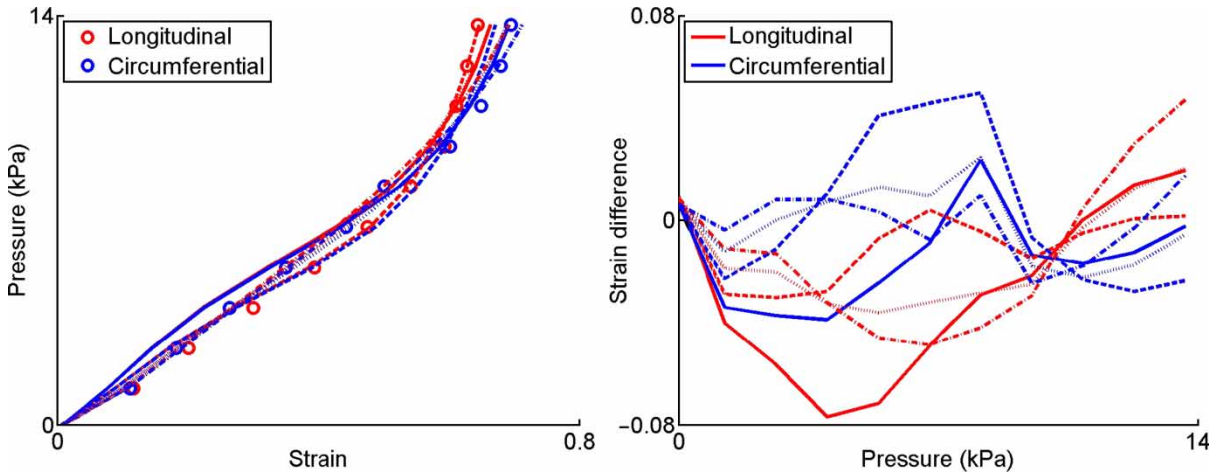


Figure 12. Final predictions resulting from local optimisation based on four different sets of initial parameter values. (left) Pressure versus strain data (symbols) and model fits (lines); (right) difference in strain (experimental strain–model strain) versus pressure. Different parameter sets are indicated with different line styles. Available in colour online.

by a local optimisation process; the local process was initialised with the parameter values obtained during the global search. The quality of agreement between model and data can be seen when viewed section by section; when viewed together (lower right pane), trends in the mechanical response between sections can be seen. In particular, the left pulmonary artery is visibly the most compliant of the three sections. It is difficult to distinguish the locking behaviour or the degree of anisotropy between the samples. Examination of the material parameters from the constitutive model is useful for these purposes.

The first group of columns in Table 2 summarises the measured thicknesses (t), the values of the material parameters (A , B , P , E_0) following the global optimisation

routine, and the accuracy of the fits (R^2_{total}). Among the 20 samples, the value of one parameter for two samples (parameter P for T3, parameter E_0 for R5) settled on the edge of the parameter domain used. For these samples, an additional set of 150 optimisation iterations was conducted with an altered parameter domain (from $1.5 \leq P \leq 2.5$ to $1.0 \leq P \leq 2.0$ for T3; from $5 \leq E_0 \leq 35$ to $20 \leq E_0 \leq 50$ for R5; other parameter ranges unchanged), to ensure the parameter domain did not impose an artificial and impactful constraint on the process. The results from these iterations are shown in the table. Also note that excellent

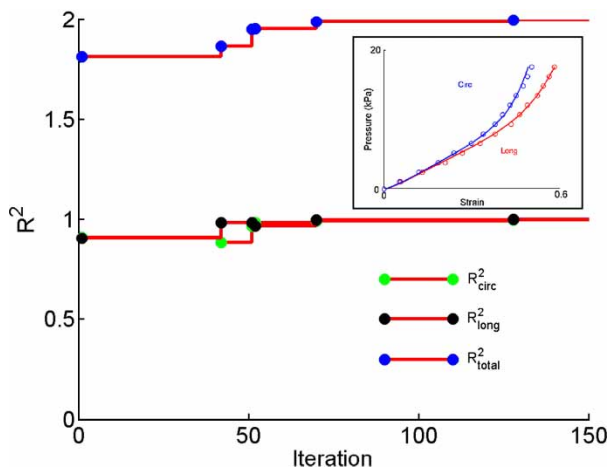


Figure 13. Progression of the solution during a global optimisation run as reflected in R^2 . Symbols indicate iterations at which a new best-fit was found. Optimisation was predefined to run for 150 iterations. (Inset) Final fit (data: symbols; model predictions: solid lines) to the pressure versus strain data. Available in colour online.

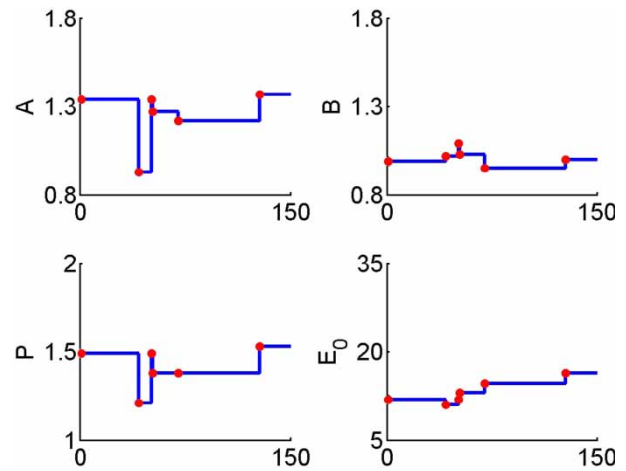


Figure 14. Evolution of material parameters corresponding to the solution progression shown in Figure 12. Ordinate axis ranges are dictated by the allowable range of the corresponding material parameter during optimisation. Because an earlier optimisation run had predicted the optimal value of P to be on the lower edge of the domain (1.5), the domain for P was reset ($1 < P < 2$) and the optimisation was performed again. Optimised values for the other parameters are in the interior of their respective domains.

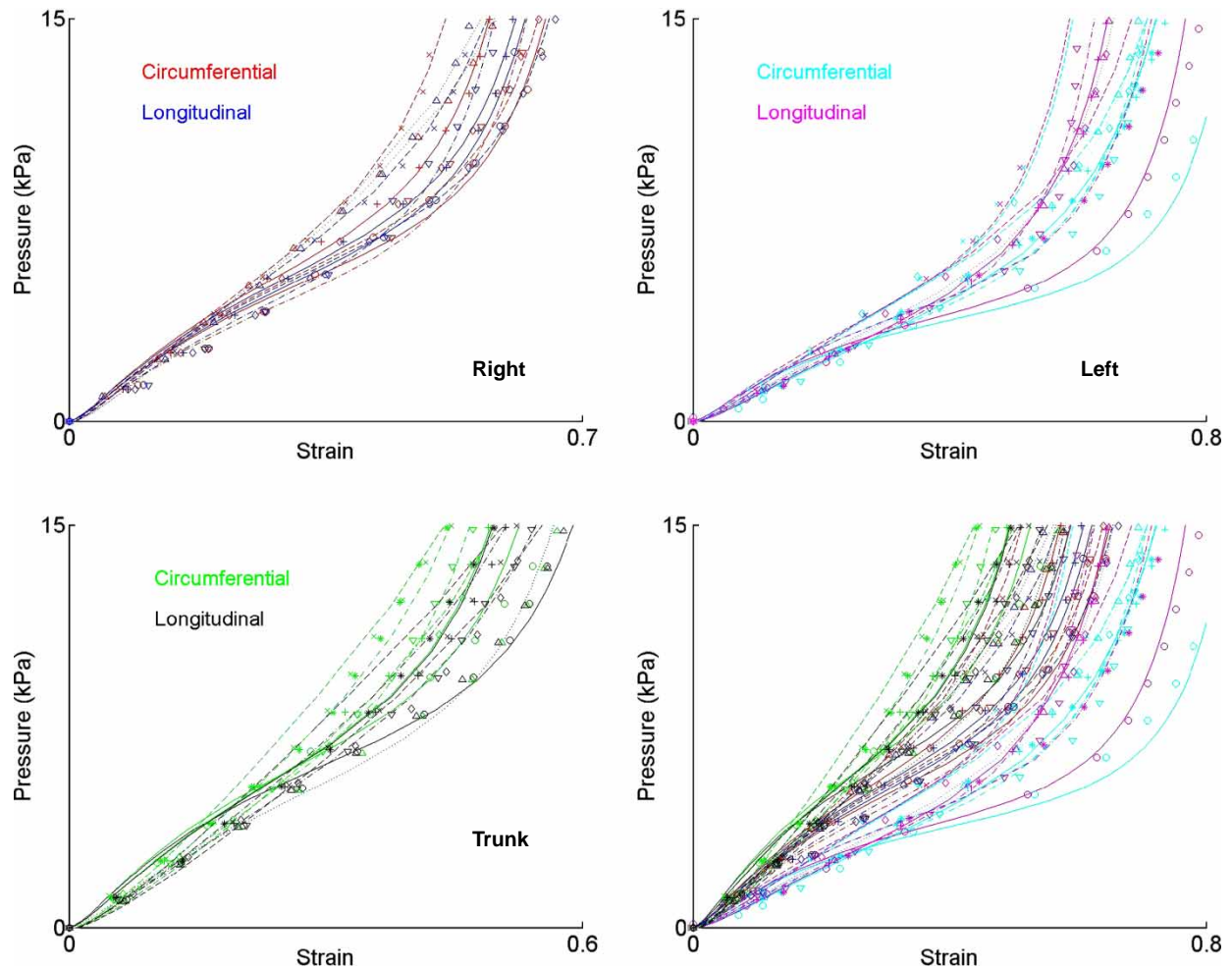


Figure 15. Experimental inflation data (symbols) and model fits (lines) from the right pulmonary artery (upper left), left pulmonary artery (upper right), and arterial trunk (lower left) of rats. (Lower right) All results are plotted together for direct visual comparison. Available in colour online.

agreement was obtained for all data sets, as the worst-case fit ($T6$, $R^2_{\text{total}} = 1.952$) is still quite good. This process was followed with a local optimisation routine for each sample, using the best case from the global optimisation as the starting point. Results from this process are also shown in Table 2, in the right group of columns. As expected, the local routine always resulted in a better fit to the experimental data. Note that results for the sample (L2) used to generate the results previously shown in Table 1 are better than the results obtained using solely local techniques, suggesting that the initial global search is an effective method for identifying the parameter subdomain.

Charts of the averaged parameter values from the combined global/local process are shown in Figure 16, along with thickness and an effective membrane stiffness ($E_0 \cdot t$). The membrane stiffness is termed ‘effective’ for several reasons. First, to be rigorous the anisotropy of the material must be considered when evaluating membrane stiffness. Secondly, the true initial stiffness from the material model

should be used, which is proportional to $E_0 \cdot t$ but dependent on other factors as well (see Appendix). However, the quantity used here is a simple way for taking into account both geometric and material effects. Figure 16 illustrates the consistency among sections of the parameters A , B and P . More significant trends are seen for E_0 , and even more so for membrane stiffness $E_0 \cdot t$. These results indicate that the left pulmonary artery is the most compliant section of the vessel, consistent with trends noted from Figure 15, and additionally that this effect is due primarily to material differences, not geometric differences.

3.4 Parameter resolution

The R^2 values associated with the upper and lower bounds on the experimental data shown in Figure 3 are as follows: $R^2_{\text{upper, long}} = 0.9857$, $R^2_{\text{lower, long}} = 0.9804$, $R^2_{\text{upper, circ}} = 0.9885$ and $R^2_{\text{lower, circ}} = 0.9853$. The acceptable reduction in the quality of the fit when quantifying resolution of the parameters is therefore $\Delta_{R^2} = 0.02$.

Table 2. Summary of results following global optimisation, and following a subsequent local optimisation.

ID	t	Following global optimisation					Following global and local optimisation				
		A	B	P	E_0	R^2_{total}	A	B	P	E_0	R^2_{total}
Left											
L1	0.1695	1.06	1.21	2.18	10.7	1.978	1.01	1.41	2.33	10.7	1.986
L2	0.1514	1.32	1.26	1.98	15.8	1.987	1.32	1.24	1.97	15.8	1.987
L3	0.1168	1.43	1.11	1.79	13.4	1.981	1.29	1.02	1.60	13.4	1.983
L4	0.1422	1.45	1.23	1.98	13.4	1.994	1.31	1.16	1.78	13.4	1.997
L5	0.0875	1.28	1.31	1.86	20.0	1.959	1.39	1.15	1.83	20.0	1.995
L6	0.1547	1.16	1.25	1.89	12.8	1.962	1.33	1.26	2.05	12.8	1.971
L7	0.1573	1.22	1.26	1.92	13.4	1.992	1.31	1.27	2.02	13.3	1.997
Avg (SD)	0.140 (0.028)	1.27 (0.14)	1.23 (0.06)	1.94 (0.12)	14.2 (3.0)	1.979 (0.014)	1.28 (0.12)	1.22 (0.12)	1.94 (0.23)	14.2 (3.0)	1.988 (0.009)
Right											
R1	0.0827	1.19	1.20	2.03	30.8	1.968	1.36	1.13	2.13	30.8	1.981
R2	0.1180	1.29	1.20	2.18	23.3	1.973	1.23	1.30	2.24	23.3	1.985
R3	0.1780	1.43	1.02	1.96	12.5	1.974	1.43	1.07	2.01	12.5	1.978
R4	0.1299	1.35	1.36	2.04	26.9	1.992	1.40	1.28	2.01	26.9	1.995
R5	0.0688	1.19	1.26	1.99	38.9	1.986	1.11	1.35	2.01	38.9	1.992
R6	0.0859	1.28	1.01	1.53	31.7	1.995	1.29	1.04	1.56	31.7	1.996
Avg (SD)	0.111 (0.040)	1.29 (0.09)	1.18 (0.14)	1.96 (0.22)	27.4 (9.0)	1.981 (0.011)	1.30 (0.12)	1.20 (0.13)	1.99 (0.23)	27.4 (9.0)	1.988 (0.008)
Trunk											
T1	0.1255	1.25	1.28	2.05	23.0	1.971	1.35	0.93	1.78	22.9	1.976
T2	0.2620	1.41	1.34	2.01	14.0	1.968	1.56	1.25	2.06	13.9	1.982
T3	0.1600	1.37	1.00	1.53	16.4	1.997	1.36	1.00	1.53	16.4	1.997
T4	0.1930	1.00	1.25	1.73	13.1	1.972	1.27	1.25	2.01	13.1	1.991
T5	0.1340	1.22	1.21	1.80	21.2	1.980	1.22	1.21	1.80	21.2	1.981
T6	0.1475	1.64	1.07	2.15	32.9	1.952	1.66	1.12	2.11	32.9	1.956
T7	0.1247	1.40	1.05	1.64	27.8	1.986	1.51	1.10	1.76	27.8	1.991
Avg (SD)	0.164 (0.049)	1.33 (0.20)	1.17 (0.13)	1.84 (0.23)	21.2 (7.4)	1.975 (0.014)	1.42 (0.16)	1.12 (0.12)	1.86 (0.21)	21.2 (7.4)	1.982 (0.014)

Results include final parameter values and overall quality of fit. Also included are the measured vessel thicknesses (t). Values are dimensionless except thickness (mm) and initial stiffness E_0 (kPa).

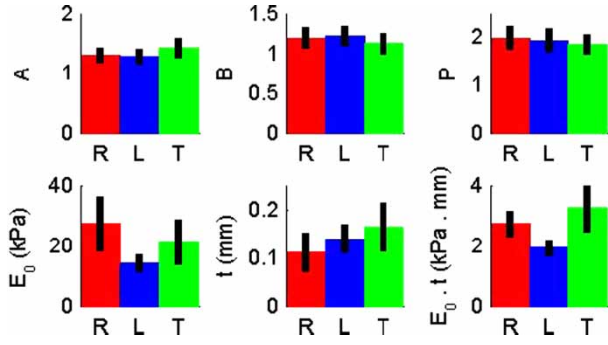


Figure 16. Optimisation results grouped by sample source (R: right pulmonary artery; L: left pulmonary artery; T: arterial trunk). Also included is the sample thickness (t) and effective membrane stiffness ($E_0 t$).

Sample L5 (Table 2) was selected as the sample data set to quantify the resolution of the material parameters; these data were previously shown in Figure 3 and were used to establish the experimental uncertainty. The resulting bounds on the material parameters are as follows, with the previously determined best fit values indicated parenthetically:

$$1.32 \leq A(1.39) \leq 1.45 \quad 1.08 \leq B(1.15) \leq 1.21$$

$$1.77 \leq P(1.83) \leq 1.91$$

$$17.4 \text{ kPa} \leq E_0(20.0 \text{ kPa}) \leq 23.0 \text{ kPa}$$

Note that these bounds are roughly symmetric, and thus the fitted parameters can be conservatively expressed as $A = 1.39 \pm 0.07$, $B = 1.15 \pm 0.07$, $P = 1.83 \pm 0.08$ and $E_0 = 20.0 \pm 3.0 \text{ kPa}$. These results indicate that the level of discretisation of the parameters that was predefined for the optimisation (0.1 for A , B and P , and 0.3 kPa for E_0) was sufficient for accurate parameter estimation. These results also suggest that though the quality of fit is improved in an absolute sense when the global search is followed with local optimisation (Table 2), the effect of the local process on the parameter values and the quality of fit is not significant when considering the experimental uncertainty.

To further explore the issue of global convergence and parameter uniqueness, again using sample L5 as a test case, the global search process was repeated using a larger number of iterations (1000). The objective of the search remained the same, namely maximising the value of R^2_{total} . However, a domain for acceptable fits was predefined and all parameter combinations that achieved this quality of fit were preserved. Recognising that the best case for L5 had R -squared values of $R^2_{\text{total}} = 1.995$ (Table 2), $R^2_{\text{long}} = 0.999$ and $R^2_{\text{circ}} = 0.996$ (not previously reported), and allowing for a tolerance on R^2_{long} and R^2_{circ} of $\Delta R^2 = 0.02$, all

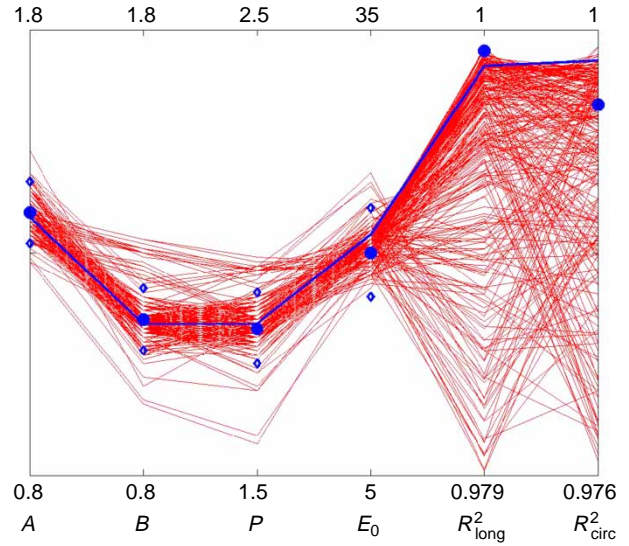


Figure 17. Parallel plot of all parameter sets that achieved agreement with the data (L5) within the experimental accuracy. Lower bounds on the R -squared values represent the minimum threshold values; bounds on the material parameters are as indicated in the figure, and represent the domain of the parameter space. Filled blue circles represent values for the best fit following the initial global search; solid blue line represents values for the best fit following the expanded global search; and blue diamonds represent range of parameter values determined using previous univariate approach. Available in colour online.

parameter sets that generated fits in which $R^2_{\text{long}} \geq 0.979$ and $R^2_{\text{circ}} \geq 0.976$ were deemed acceptable.

Results from this analysis are shown in Figure 17, represented as a parallel plot in which parameters and R^2 values for a given simulation are threaded together. Each unique thread represents an acceptable result from the optimisation process; a total of 243 threads are presented. By design, the R^2 values for each thread meet the specified tolerances. Parameter components of the threads are plotted according to the domain of the parameter space; R^2 values are plotted over the acceptable range. In addition to the threads, the best-case results from the initial global search (filled blue circles), the best-case results from the expanded search utilising 1000 iterations (solid blue line), and the resolution of the material parameters from the previous univariate approach (blue diamonds) are plotted.

4. Discussion

The goal of this study was to establish the computational formalism for estimating material parameters of nonlinear anisotropic soft tissue, including vasculature, by use of membrane inflation. This entails selection of an appropriate constitutive model, development of a computational model for the physical experiment, and use of inverse FE procedures for regressing material parameters against

experimental data. A full statistical analysis of optimisation results, both on the healthy tissue summarised here and on hypoxic tissue, and implications on the biomechanics of the vessel, are reported in a companion paper (Drexler et al. 2008). Subject to the assumption of homogeneous material properties, several structural material models are available in the literature, which in general require fewer material parameters than phenomenological models and behave physiologically over a wide range of deformation states. Additionally, orientation of the constituent fibres in such models can be derived from histological information (Holzapfel et al. 2002). Here, the four parameter model of Bischoff et al. (2002a), with parameters that correlate directly with anisotropy, nonlinearity and initial stiffness of the material response, was used.

Membrane inflation is a useful methodology for measuring constitutive information for anisotropic soft tissue, and as shown here, is conducive to inverse FE analysis for material parameter regression. While not homogeneous, the experiment can be simulated by use of a small FE model (Figure 4). For simulation of the entire domain, less than 500 elements were required, and for those tests in which the material axes aligned with the recorded profile strains, the model size was further reduced. All analyses here assumed pressure and profile strain to be the experimental data; parameter regression would be affected by inclusion of other data, including structural information through histology as well as local (crown) strains through DIC. Two-dimensional DIC has been used historically to quantify heterogeneous strain fields in cardiovascular tissue undergoing planar (2D) deformations (Beattie et al. 1998; Zhang et al. 2002), but 2D DIC does not lend itself well to curved surfaces. More recently, the methodology was advanced to enable measurement of heterogeneous, out-of-plane deformations on fully 3D specimens (Sutton et al. 2008). This technique could be applied to measure the local strain in the tissue during membrane inflation, and therefore relax the need to use global measures of strain. These techniques would be particularly relevant if assuming material homogeneity was not sufficient, for example when dealing with local altered mechanical properties due to atherosclerosis.

In cases of material heterogeneity, when local strain data are available using 2D or 3D DIC and material parameters must therefore be determined locally, the procedure outlined and incorporated here can be easily adapted. The FE model can be set up in a similar fashion, but rather than extracting profile strain to regress parameters, predictions of strain across the bubble surface can be used. Inclusion of these data will significantly compound the computational analysis, however. When using a local (gradient-based) optimisation routine, in which the number of FE simulations required per iteration is on the order of the number of free parameters, allowance

for heterogeneity would cost on the order of hundreds of simulations per iteration. For a global routine, the number of distinct parameter sets required to confidently explore the parameter space would similarly be quite large. Thus, determination of local material properties through other means, such as histology, would result in significant savings computationally.

Several different approaches were used here for parametric regression, including local and global optimisation. Local optimisation is limited because of the complex topology of the parameter space (Figure 11). Accurate fits were obtained by use of different initial parameter values (Figure 12), but a unique set of parameters was not converged upon; this result might be anticipated from the effects that material parameter perturbation has on the measured pressure versus strain results (Figure 6(b)). There is thus important sensitivity of model predictions on the initial parameter values, which can later impact statistical analysis of the results. This sensitivity could be mediated by reducing the number of free parameters (for example, fixing the value of E_0) – however, realisation of a unique solution in this case could be compromised by a lesser quality of fit.

Global optimisation techniques in general do not rely on an initial guess, but do require a large number of simulations in order to have confidence that the parameter space is fully explored. Within the context of the membrane inflation boundary value problem, in which a single iteration is not too computationally demanding, an increased number of simulations for global optimisation is not unwieldy. For this reason, global optimisation was used to estimate parameter values for data obtained from sections of rat vasculature, and the results are able to quantify differences seen qualitatively in the experimental data (Figure 16). However, as a consequence of using this global approach, a ‘best-fit’ solution cannot be guaranteed because the global parameter space is never completely explored. By allowing for more iterations per data set, the parameter space would necessarily be more fully interrogated and therefore confidence in the final parameter set would be increased. Here, 150 iterations were permitted; this was deemed sufficient because there were rarely significant changes in the values of the best-fit parameters, relative to the resolution of the parameters, beyond approximately 100 iterations. Additionally, the quality of the fits, as reflected in the R^2_{total} values, was quite good across data sets. Invoking a local optimisation process after the global search generated better fits across all data sets (Table 2), but in all cases the improvement in R^2_{total} did not exceed the estimated uncertainty in the raw data. Thus, in practice this local search is not justified.

Taking into account the complexity of the response surface, the computational cost of a single FE analysis of membrane inflation, the overall quality of fit that can be obtained with the orthotropic hyperelastic model used

here, and the uncertainty in the experimental data, this study suggests that material parameters can be estimated most efficiently using global optimisation, in this case the Sherpa algorithm. Confidence in the uniqueness of the final parameter set will increase with the number of iterations performed, but cannot be guaranteed in an absolute sense because of the nonlinear nature of the problem. Inclusion of data from additional modes of deformation, such as planar biaxial deformation, could also be used to increase confidence in the converged material parameters, in addition to establishing the predictive capabilities of the mathematical model. Acquisition of such data is beyond the scope of this study, but should be considered in future work.

Uniqueness of material parameters is a key issue within any parametric regression process, and can be difficult to address conclusively as computational and experimental models increase in complexity. Several steps here, applied to a representative data set (L5), suggest that the optimisation path utilised here, in conjunction with the material model and experimental data sets, gives rise to a unique set of parameters within a margin of uncertainty. In particular, by perturbing each parameter systematically until the experimental uncertainty was exceeded (termed here the univariate approach, as coupling between parameters is not considered), and by performing a global search with an increased number of iterations (termed here the multivariate approach), the resolution of the material parameters was roughly quantified. The global search (Figure 17) produced acceptable parameter sets that were outside the bounds established through the univariate approach. This is likely a reflection of coupling between the parameters in terms of the system response. In any case, the absolute thresholds in parameter resolution from the global search, permitting 1000 iterations as compared to 150 iterations in the earlier analysis, are generally no more than a factor of two greater than from the systematic search, with better agreement obtained for parameters A and E_0 . More importantly, the threads suggest that there is a single connected domain within the parameter space that yields adequate results. Thus, the domain can be considered unique, with an objective best fit lying within that domain.

There are several limitations to the work here, associated with the choice of material model and experimental data set. Inelastic material response, particularly time-dependency (viscoelasticity), is not represented in the experimental data and therefore not included in the constitutive model. Additionally, both the experimental measurements and modelling approach assume material homogeneity. Finally, material testing and computational modelling both assume an initial state that lacks residual stress, whereas physiological prestresses are known to exist in cardiovascular tissue. More complex measurement techniques can be used to draw out each of these effects, and therefore motivate use of more

advanced material models; the coupling between data and model could then proceed as presented here, namely by examining parameter sensitivity, selecting an optimisation approach and performing the inverse analysis.

In summary, a protocol for global optimisation of material parameters from a four parameter nonlinear anisotropic constitutive model using inverse FE analysis based on membrane inflation has been established. This procedure has been applied to a baseline set of experimental data, and can be used to quantify differences in mechanical response due to disease, sample location, or other variables. With this framework in place, expansion to include additional experimental data (local surface strain or histology) or more complex constitutive models (such as viscoelasticity) can be achieved in order to more fully understand vessel biomechanics.

Acknowledgements

Contribution of the National Institute of Standards and Technology, an agency of the US government; not subject to copyright in the USA.

Note

1. Product names are provided for completeness of description; their inclusion neither constitutes nor implies endorsement by NIST.

References

- Augenstein KF, Cowan BR, LeGrice IJ, Nielsen PMF, Young AA. 2005. Method and apparatus for soft tissue parameter estimation using tissue tagged magnetic resonance imaging. *J Biomech Eng.* 127(1):148–157.
- Beattie D, Xu C, Vito R, Glagov S, Whang MC. 1998. Mechanical analysis of heterogeneous, atherosclerotic human aorta. *J Biomech Eng.* 120:602–607.
- Bergström JS, Kurtz SM, Rimnac CM, Edidin AA. 2002. Constitutive modeling of ultra-high molecular weight polyethylene under large-deformation and cyclic loading conditions. *Biomaterials* 23:2329–2343.
- Bischoff JE, Arruda EM, Grosh K. 2002a. A microstructurally based orthotropic hyperelastic constitutive law. *J Appl Mech.* 69:570–579.
- Bischoff JE, Arruda EM, Grosh K. 2002b. Finite element simulations of orthotropic hyperelasticity. *Finite Elements Anal Des.* 38(10):983–998.
- Bischoff JE, Arruda EM, Grosh K. 2004. A rheological network model for the continuum anisotropic and viscoelastic behavior of soft tissue. *Biomech Model Mechanobiol.* 3(1): 56–65.
- Cox MAJ, Driessen NJB, Bouten CVC, Baaijens FPT. 2006. Mechanical characterization of anisotropic planar biological soft tissues using large indentation: a computational feasibility study. *J Biomech Eng.* 128:428–436.
- Delfino A, Stergiopoulos N, Moore Jr. JE, Meister J-J. 1997. Residual strain effects on the stress field in a thick wall finite element model of the human carotid bifurcation. *J Biomech.* 30(8):777–786.

- Demiray H, Vito RP. 1991. A layered cylindrical shell model for an aorta. *Int J Engng Sci.* 29(1):47–54.
- Dixon SA, Heikes RG, Vito RP. 2003. Constitutive modeling of porcine coronary arteries using designed experiments. *J Biomech Eng.* 125:274–279.
- Drexler ES, Slifka AJ, Wright JE, McCowan CN, Finch DS, Quinn TP, McColskey JD, Ivy DD, Shandas R. 2003. An experimental method for measuring mechanical properties of rat pulmonary arteries verified with latex. *J Res NIST.* 108:183–191.
- Drexler ES, Quinn TP, Slifka AJ, McCowan CN, Bischoff JE, Wright JE, Ivy DD, Shandas R. 2007. Comparison of mechanical behavior among the extrapulmonary arteries from rats. *J Biomech.* 40:812–819.
- Drexler ES, Bischoff JE, Slifka AJ, McCowan CN, Quinn TP, Shandas R, Ivy DD, Stenmark KR. 2008. Stiffening of the extrapulmonary arteries in chronic hypoxic pulmonary hypertension. *J Res NIST* (accepted).
- Erdemer A, Viveiros ML, Ulbrecht JS, Cavanagh PR. 2006. An inverse finite-element model of heel-pad indentation. *J Biomech.* 39:1279–1286.
- Fung YC. 1993. *Biomechanics: mechanical properties of living tissues.* New York: Springer-Verlag.
- Gleason RL, Wilson E, Humphrey JD. 2007. Biaxial biomechanical adaptations of mouse carotid arteries cultured at altered axial extension. *J Biomech.* 40:766–776.
- Holzapfel GA, Gasser TC, Ogden RW. 2000. A new constitutive framework for arterial wall mechanics and a comparative study of material models. *J Elast.* 61:1–48.
- Holzapfel GA, Gasser TC, Stadler M. 2002. A structural model for the viscoelastic behavior of arterial walls: continuum formulation and finite element analysis. *Eur J Mech A/Solids.* 21:441–463.
- Holzapfel GA, Gasser TC, Ogden RW. 2004. Comparison of a multi-layer structural model for arterial walls with a Fung-type model, and issues of material stability. *J Biomech Eng.* 126:264–275.
- Hsu FPK, Schwab C, Rigamonti D, Humphrey JD. 1994. Identification of response functions from axisymmetric membrane inflation tests: implication for biomechanics. *Int J Solids Struct.* 31:3375–3386.
- Humphrey JD. 1995. Mechanics of the arterial wall: review and directions. *Crit Rev Biomed Eng.* 23(1/2):1–162.
- Humphrey JD, Vawter DL, Vito RP. 1987. Quantification of strains in biaxially tested soft tissues. *J Biomech.* 20:59–65.
- Humphrey JD, Strumpf RK, Yin FCP. 1990. Determination of a constitutive relation for passive myocardium: I. A new functional form. *J Biomech Eng.* 112:333–339.
- Kyriacou SK, Humphrey JD. 1997. Inverse finite element characterization of nonlinear hyperelastic membranes. *J Appl Mech.* 64:257–262.
- Lei F, Szeri AZ. 2007. Inverse analysis of constitutive models: biological soft tissues. *J Biomech.* 40:936–940.
- Malcolm DTK, Nielsen PMF, Hunter PJ, Charette PG. 2002. Strain measurements in biaxially loaded inhomogeneous, anisotropic elastic membranes. *Biomech Mod Mechanobiol.* 1(3):197–210.
- Nair AU, Taggart DG, Vetter FJ. 2007. Optimizing cardiac material parameters with a genetic algorithm. *J Biomech.* 40:1646–1650.
- Ohashi T, Abe H, Matsumoto T, Sato M. 2005. Pipette aspiration technique for the measurement of nonlinear and anisotropic mechanical properties of blood vessel walls under biaxial stretch. *J Biomech.* 38:2248–2256.
- Press WH, Teukolsky SA, Vetterling WT, Flannery BP. 1992. *Numerical recipes in C: the art of scientific computing.* 2nd ed. Cambridge: Cambridge University Press.
- Slifka AJ, Drexler ES, Wright JE, Shandas R. 2006. Bubble-test method for synthetic and bovine vascular material. *J Biomech.* 39:1939–1942.
- Sutton MA, Ke X, Lessner SM, Goldbach M, Yost M, Zhao F, Schreier HW. 2008. Strain field measurements on mouse carotid arteries using microscopic three-dimensional digital image correlation. *J Biomed Mater Res.* 84A:178–190.
- VanBavel E, Siersma P, Spaan JAE. 2003. Elasticity of passive blood vessels: a new concept. *Am J Physiol Heart Circ Physiol.* 285:H1986–H2000.
- Vito RP, Dixon SA. 2003. Blood vessel constitutive models – 1995–2002. *Annu Rev Biomed Eng.* 5:413–439.
- Zhang D, Eggleton CD, Arola DD. 2002. Evaluating the mechanical behavior of arterial tissue using digital image correlation. *Exp Mech.* 42(4):409–416.
- Zhang Y, Dunn ML, Drexler ES, McCowan CN, Slifka AJ, Ivy DD, Shandas R. 2005. A microstructural hyperelastic model of pulmonary arteries under normo- and hypertensive conditions. *Ann Biomed Eng.* 33(8):1042–1052.

Appendix

The constitutive model is a mathematical representation of the tissue structure idealisation shown (in two dimensions) in Figure A1. Original derivation of the model can be found elsewhere (Bischoff et al. 2002a); here, it is reformulated in terms of a different set of independent material parameters that each have a clearer effect on the predicted material response (Figure 3).

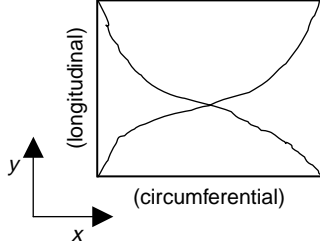


Figure A1. Two-dimensional representation of the structural basis for the orthotropic constitutive model used here. Parameters A and B reflect fibre alignment along the circumferential and longitudinal directions, respectively; P reflects the amount of fibre crimp; and E_0 reflects the initial stiffness of the unit cell.

The strain energy function for the material is given by

$$W = W_0 + \frac{E_0}{4} \left[P^2 \sum_{i=1}^4 \left(\frac{\rho^{(i)}}{P^2} \beta^{(i)} + \ln \frac{\beta^{(i)}}{\sinh \beta^{(i)}} \right) - \frac{\beta_P}{P} \ln \left(\lambda_a^{A^2 P^2} \lambda_b^{B^2 P^2} \lambda_c^{C^2 P^2} \right) \right],$$

where $\rho^{(i)} = \sqrt{\mathbf{P}^{(i)\text{T}} \cdot \mathbf{C} \cdot \mathbf{P}^{(i)}}$, $\lambda_a = \sqrt{\mathbf{a}^{\text{T}} \cdot \mathbf{C} \cdot \mathbf{a}}$, $\lambda_b = \sqrt{\mathbf{b}^{\text{T}} \cdot \mathbf{C} \cdot \mathbf{b}}$, $\lambda_c = \sqrt{\mathbf{c}^{\text{T}} \cdot \mathbf{C} \cdot \mathbf{c}}$, $\beta^{(i)} = L^{-1}(\rho^{(i)}/P^2)$, and $C = \sqrt{4 - A^2 - B^2}$.

$$\mathbf{H} = E_0 \begin{bmatrix} P'A^4 + \frac{\beta_P P}{2} A^2 & P'A^2 B^2 & P'A^2 C^2 & 0 & 0 & 0 \\ P'A^2 B^2 & P'B^4 + \frac{\beta_P P}{2} B^2 & P'B^2 C^2 & 0 & 0 & 0 \\ P'A^2 C^2 & P'B^2 C^2 & P'C^4 + \frac{\beta_P P}{2} C^2 & 0 & 0 & 0 \\ 0 & 0 & 0 & P'A^2 B^2 & 0 & 0 \\ 0 & 0 & 0 & 0 & P'A^2 C^2 & 0 \\ 0 & 0 & 0 & 0 & 0 & P'B^2 C^2 \end{bmatrix}.$$

The second PK stress tensor $\mathbf{S} = \partial W / \partial \mathbf{E}$ is

$$\mathbf{S} = \frac{E_0}{4} \left[\sum_{i=1}^4 \left(\frac{\mathbf{P}^{(i)} \otimes \mathbf{P}^{(i)}}{\rho^{(i)}} \beta^{(i)} \right) - \beta_P P \left(\frac{A^2}{\lambda_a^2} \mathbf{a} \otimes \mathbf{a} + \frac{B^2}{\lambda_b^2} \mathbf{b} \otimes \mathbf{b} + \frac{C^2}{\lambda_c^2} \mathbf{c} \otimes \mathbf{c} \right) \right].$$

The elasticity tensor $\mathbf{H} = \partial^2 W / \partial \mathbf{E}^2$ is

$$\mathbf{H} = \frac{E_0}{4} \sum_{i=1}^4 \left(\frac{1}{(\rho^{(i)})^3} \left[\rho^{(i)} \left(\frac{\partial \beta}{\partial \rho} \bigg|_{\rho=\rho^{(i)}} \right) - \beta^{(i)} \right] \mathbf{P}^{(i)} \otimes \mathbf{P}^{(i)} \otimes \mathbf{P}^{(i)} \otimes \mathbf{P}^{(i)} \right) + \frac{E_0 \beta_P P}{2} \left(\frac{A^2}{\lambda_a^4} \mathbf{a} \otimes \mathbf{a} \otimes \mathbf{a} \otimes \mathbf{a} + \frac{B^2}{\lambda_b^4} \mathbf{b} \otimes \mathbf{b} \otimes \mathbf{b} \otimes \mathbf{b} + \frac{C^2}{\lambda_c^4} \mathbf{c} \otimes \mathbf{c} \otimes \mathbf{c} \otimes \mathbf{c} \right),$$

where

$$\frac{\partial \beta}{\partial \rho} = \frac{1}{P^2} \left(1 - \coth^2 \beta + \frac{1}{\beta^2} \right)^{-1}.$$

The elasticity tensor at zero deformation reduces to

$$\begin{aligned} \mathbf{H}_0 = & E_0 P' [A^4 \mathbf{a} \otimes \mathbf{a} \otimes \mathbf{a} \otimes \mathbf{a} + B^4 \mathbf{b} \otimes \mathbf{b} \otimes \mathbf{b} \otimes \mathbf{b} + C^4 \mathbf{c} \otimes \mathbf{c} \otimes \mathbf{c} \otimes \mathbf{c}] \\ & + \frac{E_0 \beta_P P}{2} [A^2 \mathbf{a} \otimes \mathbf{a} \otimes \mathbf{a} \otimes \mathbf{a} + B^2 \mathbf{b} \otimes \mathbf{b} \otimes \mathbf{b} \otimes \mathbf{b} + C^2 \mathbf{c} \otimes \mathbf{c} \otimes \mathbf{c} \otimes \mathbf{c}] \\ & + E_0 P' A^2 B^2 [\mathbf{a} \otimes \mathbf{a} \otimes \mathbf{b} \otimes \mathbf{b} + \mathbf{b} \otimes \mathbf{b} \otimes \mathbf{a} \otimes \mathbf{a} + \mathbf{a} \otimes \mathbf{b} \otimes (\mathbf{b} \otimes \mathbf{a} + \mathbf{a} \otimes \mathbf{b}) \\ & + \mathbf{b} \otimes \mathbf{a} \otimes (\mathbf{a} \otimes \mathbf{b} + \mathbf{b} \otimes \mathbf{a})] + E_0 P' A^2 C^2 [\mathbf{a} \otimes \mathbf{a} \otimes \mathbf{c} \otimes \mathbf{c} + \mathbf{c} \otimes \mathbf{c} \otimes \mathbf{a} \otimes \mathbf{a} \\ & + \mathbf{a} \otimes \mathbf{c} \otimes (\mathbf{c} \otimes \mathbf{a} + \mathbf{a} \otimes \mathbf{c}) + \mathbf{c} \otimes \mathbf{a} \otimes (\mathbf{a} \otimes \mathbf{c} + \mathbf{c} \otimes \mathbf{a})] \\ & + E_0 P' B^2 C^2 [\mathbf{b} \otimes \mathbf{b} \otimes \mathbf{c} \otimes \mathbf{c} + \mathbf{c} \otimes \mathbf{c} \otimes \mathbf{b} \otimes \mathbf{b} + \mathbf{b} \otimes \mathbf{c} \otimes (\mathbf{c} \otimes \mathbf{b} + \mathbf{b} \otimes \mathbf{c}) \\ & + \mathbf{c} \otimes \mathbf{b} \otimes (\mathbf{b} \otimes \mathbf{c} + \mathbf{c} \otimes \mathbf{b})], \end{aligned}$$

where

$$P' \equiv \frac{P}{16} \left(P \frac{\partial \beta}{\partial \rho} \bigg|_{\rho=P} - \beta_P \right).$$

This fourth-order tensorial equation can be cast in terms of a two-dimensional stiffness matrix in the $(\mathbf{a}, \mathbf{b}, \mathbf{c})$ coordinate system,